Nonadiabatic molecular dynamics analysis of hybrid Dion–Jacobson 2D leads iodide perovskites: A Nonadiabatic Molecular Dynamics Study

Ying Wang, Laurent Pedesseau, Claudine Katan, Jacky Even, Oleg Prezhdo, Sergei Tretiak, Dibyajyoti Ghosh, Amanda Neukirch

Nonadiabatic molecular dynamics analysis of hybrid Dion-Jacobson 2D lead Iodide perovskites

Ying Wang† ‡, Laurent Pedesseau‖, Claudine Katan▽, Jacky Even‖, Oleg V. Prezhdo†, Sergei Tretiak‡, Dibyajyoti Ghosh‡§#*, Amanda J. Neukirch‡*

† Department of Chemistry, University of Southern California, Los Angeles, California 90089, United States

‡ Theoretical Physics and Chemistry of Materials, Los Alamos National Laboratory, Los Alamos, New Mexico 87545, United States

‖ Univ Rennes, INSA Rennes, CNRS, Institut FOTON, UMR 6082, Rennes F-35000, France

▽ Univ Rennes, ENSCR, INSA Rennes, CNRS, ISCR (Institut des Sciences Chimiques de Rennes), UMR 6226, Rennes F-35000, France

§ Center for Nonlinear Studies, Los Alamos National Laboratory, Los Alamos, New Mexico 87545, United States

Department of Materials Science and Engineering and Department of Chemistry, Indian Institute of Technology, Delhi, New Delhi 110016, India

* Corresponding Authors: dibyajnc@gmail.com; ajneukirch@lanl.gov

Abstract:

The past 6 years have witnessed the rapid growth of interest in Dion-Jacobson (DJ) phase two dimensional (2D) hybrid halide perovskites as optoelectronic materials with considerable intrinsic stability. The precise relationships between structural variations and the resulting charge carrier dynamics at finite temperature in these materials are key to practical applications and are not yet completely understood. Here, we study 3-(aminomethyl) piperidinium (3AMP) and 4-(aminomethyl) piperidinium (4AMP) spacer cation-based lead iodide DJ-phase systems and find these spacer cations to have a profound impact on the structural dynamics. Particularly, large conformational dynamics of the 3AMP based perovskite compared to that of the 4AMP at room temperature leads to pronounced state energy fluctuation near band edges and further results in a shorter quantum coherence. The faster quantum decoherence of the 3AMP spacer-based perovskite underpins a longer nonradiative lifetime, offering insight into its superior performance as an optoelectronic material. This work sheds light on the relationship between structural fluctuations and charge carrier dynamics that can help in designing 2D perovskites with superior photo-physical properties.

Conventional three-dimensional (3D) halide organic-inorganic perovskites (HOIPs) have achieved solar cells with power conversion efficiencies (PCE) exceeding 25%[1-2]. However, they are often unstable to moisture, light, and heat[3-7]. 3D HOIPs are also limited in the choice of organic moiety due to structural stability as defined by the empirical Goldschmidt tolerance factor[8-9]. In contrast, two-dimensional (2D) HOIPs do not face the same intrinsic restriction for choosing spacer cations. Consequently, 2D perovskites can incorporate bulky organic cations such as (butylammonium, BA^+, phenethylammonium, PEA^+, and 3-(aminomethyl) piperidinium, 3AMP, 4-(aminomethyl) piperidinium, 4AMP) that act as the spacer molecules and provide a steric barrier for surface water intrusions[10-12]. With versatile tunings of interlayer cations endowing these 2D perovskites with rich optoelectronic properties[13-16], they have become a promising class of materials for solar cells and other optoelectronic applications. Despite improved structural properties, initially, 2D HOIPs struggled to compete with other high-performing optoelectronic materials, due to reduced and anisotropic charge transport[17-18] caused by the bulky organic spacer layers. However, an intense research effort has partially addressed this limitation and the PCE of 2D perovskites has improved from 4.73%[19] to 18%[20-21] recently. The enhanced efficiency of 2D halide perovskite devices results from better intrinsic properties of the materials which are systematically engineered during and after synthesis [20, 22-23]. Further improvements in the carrier dynamics and PCE will require an in-depth understanding of these materials that can be supported by *ab initio* investigations.

Currently, 2D Ruddlesden–Popper[14, 24] (RP), and Dion–Jacobson[25-28] (DJ) phase perovskites are two promising classes of materials for optoelectronic devices. RP phases have been around for decades and are easier to synthesize. DJ phase perovskites are much newer and harder to synthesize, however have realized an explosive growth of PCE from 7.32%[29] to 15.6%[30] within only one year indicating they are a more compelling path forward. Both phases exhibit high moisture resistance and tunable optoelectronic properties[31-32]. 2D perovskites are usually defined with the formula $(A')_m(A)_{n-1}B_nX_{3n+1}$, where A′ can be divalent (m = 1) or monovalent (m = 2) cation that forms a bilayer or monolayer connecting the perovskite $(A)_{n-1}B_nX_{3n+1}$ 2D sheets, where n indicates the layer thickness of metal halide sheets that can be adjusted by tuning precursor composition. RP- and DJ-phase perovskites have m=2 and m=1, respectively. 'A' represents a short monocationic molecule or atom (e.g. Cs^+), 'B' is the divalent metal atom (Pb, Sn, Ge), and 'X' is the halide (Cl, Br, I). The structural difference between these two phases is shown in a relative stacking of the layers: the RP phase perovskites have two monovalent spacer cations. Here due to the large interlayer distance and weak van der Waals interaction between spacer monocations, the interlayer conductivity is severely restricted. In contrast, the interlayer gap is bridged by only one short bivalent spacer cation in DJ perovskites, where the inorganic layers stack exactly on top of each other and the van der Waals gap between adjacent interlayer cations disappears. This introduces fewer degrees of freedom into the structure, making the inorganic layers closer to each other, and resulting in better out-of-plane charge transport properties and improved stability.[33] Recently, with a smaller bandgap for the same value of n and a shorter interlayer distance, compared to the RP phase. Despite showing more potential for optoelectronic applications compared to the RP phase perovskites, due to both DJ phase's newness to the community and their more difficult synthesis, systematic investigations into the fundamental aspects and systematic investigations into the optimization of DJ phase perovskite devices are nearly untouched.

Here, we perform an in-depth comparison of structural and electronic properties that dominate the photophysical properties of two different DJ phase perovskites, (3AMP) $(MA)_3Pb_4I_{13}$ and (4AMP)$(MA)_3Pb_4I_{13}$. To consider dynamical processes influencing charge carriers at ambient conditions, we employ *ab initio* real-time time-dependent density functional theory (DFT) and nonadiabatic molecular dynamics (NAMD) modeling. We find that different spacer cations significantly impact the thermal structural variations in these halide perovskites. (3AMP) $(MA)_3Pb_4I_{13}$ has larger structural fluctuations causing faster quantum dephasing compared to (4AMP) $(MA)_3Pb_4I_{13}$. Comparable nonadiabatic coupling with faster quantum dephasing leads to a long carrier lifetime in 3-AMP based perovskites compared to 4-AMP based perovskites. In addition, electron-phonon coupling in DJ phases may have a decisive impact on the reduction of extrinsic non-radiative recombination and carrier trapping as shown previously for RP phases[34].

We start our simulations with previously reported structures[29] as the initial geometries for (3AMP)$(MA)_3Pb_4I_{13}$ and (4AMP)$(MA)_3Pb_4I_{13}$. In these geometries, every slab with four layers of $[PbI_6]^{4-}$ octahedra remain separated by a layer of 3AMP or 4AMP dications. We further refer to these materials as **3AMP** and **4AMP** perovskites, respectively. Due to the presence of light atoms and thermally activated molecular dynamics, X-ray diffraction-based structural determination techniques cannot discern the exact conformation of the asymmetric organic cations in between the two inorganic layers with absolute certainty, as well as structural distortions related to inversion symmetry breaking. As a result, recent studies have reported two different interlayer cation alignments in the spacer region[35-36]. Thus, we initially consider both spacer-cation conformations (Fig. 1 (c) - (f) and Supplemental Fig. S1) because these two conformations may coexist. In these two conformations, the nearest-neighbor spacer cations (that is 3AMP or 4AMP molecules) along the b-axis remain aligned (Fig. 1(c), (d)) or anti-aligned (Fig. 1(e), (f)) to each other in the ab-plane. Our structure optimizations (see SI Computational Methods) with fixed cell parameters and without any constraints on atomic positions reveal that for both perovskites, the aligned and anti-aligned structures are energetically very similar as tabulated in Supplemental Table S1. The experimental bandgap values[29] of these two perovskites are 1.87 eV and 1.89 eV respectively. Simulated band gap values without considering spin-orbit coupling (SOC) of aligned structures and anti-aligned structures are shown in Table 1. The band gap values without SOC correction are 10's of meV away from the experimentally measured data for the **4AMP** system. This seemingly excellent agreement is actually due to a well-documented mutual cancelation of errors that stems from leaving out spin-orbit coupling[37-42] (band gap narrowing) and electronic many-body interactions[43] (band gap widening). Unfortunately, with 260 atoms per simulation cell, the inclusion of SOC is prohibitive for many of the calculations in this work (see SI Computational Methods). Nonetheless, with or without the inclusion of SOC correction, we notice two important trends from our simulations. First, the calculated band gap is largely insensitive to the cation orientation in the case of the **4AMP** perovskite, however, the band gap of **3AMP** significantly changes with the alignment of its cations. It is known experimentally that the shape of the 3AMP cation by comparison to its 4AMP counterpart is at the origin of strain accumulation in the corresponding DJ compounds or intermediate n values[27-28]. Second, computational findings for the anti-aligned conformation of **3AMP** matches closely with the available experimental structural data. To analyze structural features, we rely on previous extensive work relating the backbone structure to the electronic properties of 2D perovskites[10, 15, 28, 44]. First, we note that the average

Pb-I-Pb bond angle and Pb-I bond length (Supplemental Table S2) for both **3AMP** and **4AMP** perovskites do not change significantly between the aligned and anti-aligned structures. In order to quantify how much of the band gap opening observed for **3AMP** (Table 1) is cation orientation vs perovskite backbone, we place the anti-aligned cations in the perovskite backbone that was optimized for the aligned **3AMP** and optimized only the interlayer organic atoms while keeping the perovskite atoms frozen. The band gap from this test is 1.84 eV, indicating that the cation orientation is almost entirely responsible for the band gap opening that matches experiment. Finally, inspection of non-covalent hydrogen-bonding (H-bonding) shows that the average H-bond length between inorganic Pb_4I_{13} layers and spacer cations is shorter in the anti-aligned conformations (Supplemental Table S3) compared to the aligned ones. This further indicates that the anti-aligned structures have stronger H–bonding interactions that stabilize this conformation.

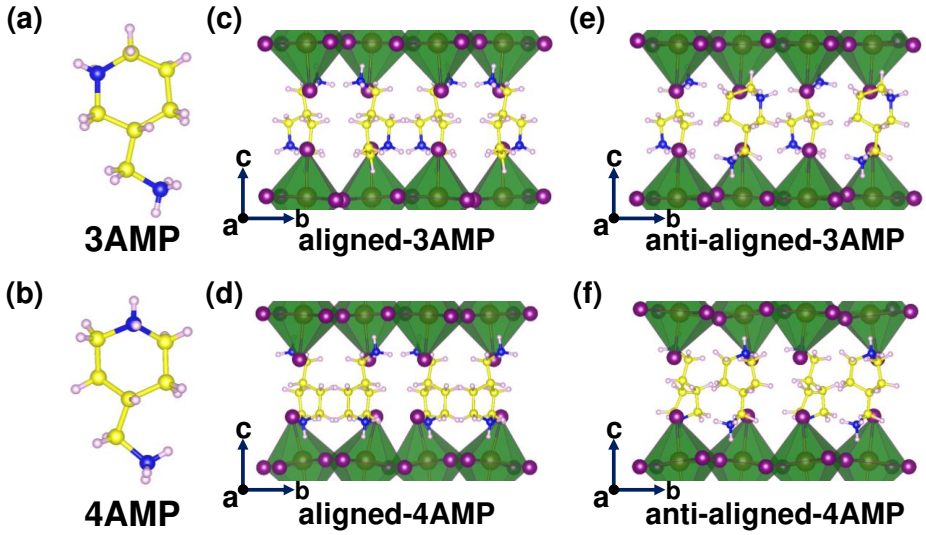

Figure 1. Molecular structure of (a) 3AMP and (b) 4AMP spacer cations (here, in order to present the structures of these two cations clearly, we show the 3AMP and 4AMP cations without coordination directions). Optimized structures of aligned (c) $(3AMP)(MA)_3Pb_4I_{13}$ (**3AMP**) and (d) $(4AMP)(MA)_3Pb_4I_{13}$ (**4AMP**) perovskites. (e) and (f) show their anti-aligned conformations, respectively. To emphasize the spacer cations, Pb and I atoms are shown with smaller radii. Yellow, blue, canyon, purple, and pink represent C, N, Pb, I, and H atoms, respectively. The green octahedra represent the Pb-I octahedra.

Table 1. Calculated band gap values (without SOC) of aligned/anti-aligned **3AMP** and **4AMP** perovskites. BG refers to Bandgap, which is the same for the following tables.

species	aligned-**3AMP**	aligned-**4AMP**	anti-aligned-**3AMP**	anti-aligned-**4AMP**
BG (eV)	1.42	1.86	1.83	1.89

Since the cation alignment orientation is of interest to the community, and somewhat surprisingly important to obtain consistent basic electronic structure for **3AMP**, we explore this factor in more

detail. First, we examine the dipole moments for the two molecules (see SI Computational Methods). As shown in Supplemental Table S4, when the interlayer cations are aligned, the dipole moments of two nearest-neighbor cations for **3AMP** and **4AMP** are 9.09 and 6.06 Debye, respectively. In these aligned perovskites, the dominant part of the dipole moments of interlayer cations lies along the out-of-plane direction (c axis), pointing to the aminomethyl. This aminomethyl is more positively charged than $(NH_2)^+$ within the piperidinium based on the dipole moment direction. When inspecting the partial charge density of the band edge states for the aligned systems we do observe noticeable asymmetries for **3AMP** and **4AMP** in Supplemental Figure S2. **3AMP** are very asymmetric within the perovskite layers with the electron and hole wavefunctions being separated. This separation rationalizes the erroneously calculated low band gap, owing to a known problem of DFT when dealing with charge-separated states[45-46]. When the interlayer cations are anti-aligned, the dipole moment of two nearest-neighbor cations for **3AMP** and **4AMP** is 1.01 and 4.15 Debye, respectively. For anti-aligned structures, dipoles are directed within the ab-plane, which leads to a more symmetric partial charge distribution (Supplemental Figure S3). This large difference in the dipole moment between the aligned and anti-aligned two nearest-neighbor **3AMP** rationalizes the band gap mismatch between the aligned conformation and the experimentally measured band gap in this system. These results demonstrate that to accurately model these asymmetric spacer cation-based systems, it is very important to check their possible mutual orientations, corresponding energetics, and electronic properties. As such for subsequent calculations, we only consider the anti-aligned conformations of both DJ phase perovskites. While we show that for the **3AMP** system the cations need to be in an anti-aligned configuration due to limitations of DFT, the actual orientation of the cations in the experiment remains an open question.

Experimentally, **3AMP** and **4AMP** bandgaps (around 1.9 eV) are in the visible light range. Calculated band structures are shown in Supplemental Figure S4. I-5p orbitals dominate the valence band maximum (VBM) and Pb-6p orbitals dominate the conduction band minimum (CBM) for both perovskites as illustrated in Supplemental Figures S3 and S5. There is still a slight orbital asymmetry for the anti-aligned structures in the charge density distributions that is most likely arises from the residual dipole moments of these two systems. This is likely due to variations in the octahedral tilting angles along the stacking axis and preventing perfect inversion symmetry[47]. To get some insight into the charge carrier transport, we calculated the effective masses from the band-edge structures computed including SOC. As shown in Supplemental Table S5, the effective masses of electrons and holes along with the stacking direction range from 0.22 m_0 to 0.63 m_0, which is greater than the effective masses of in-plane carriers (0.17-0.39 m_0). In Supplemental Figure S2 (a, b), bands near CBM and VBM look almost flat due to the short distance between Γ and B in the reciprocal space. However, if we zoom in to the part of Γ→B (see Supplemental Figure S6), we can observe clear curvatures, suggesting that these DJ-phase perovskites have better charge transport along the stacking direction compared to other 2D perovskites[48], which typically have very large effective masses and almost flat dispersion curves compared to their 3D counterparts along the stacking axis[15]. When we include SOC corrections, two bands near the VBM of **3AMP** remain nearly doubly degenerate, Figure S6 (a). The substantially lighter effective hole of one of the bands near the VBM of this perovskite can improve the charge mobility along the stacking direction significantly compared with that of **4AMP**.

Once 3AMP and 4AMP are heated up, such that the following ab initio molecular dynamics

(AIMD) trajectory remains stable at 300±5 K for 5 ps , we observe several important structural features. From the T=0K optimized geometries, we find that the averaged $[PbI_6]^{4-}$ octahedra of **4AMP** become more distorted compared to that of **3AMP**. Further, **3AMP** has smaller time-averaged Pb-I-Pb bond angle deviations from 180° over the simulation cell (Table S6). With a temperature increase, there is less octahedral distortion for both materials, however, **4AMP** remains the more distorted as seen from the Pb-I-Pb bond angle, Supplemental Table S6. The asymmetry in the VBM and CBM charge densities that were observed at equilibrium balances out at RT, and charge densities become evenly distributed across the first and third sublayers as shown in Figure 2. Another point to note is the modification of the Jahn-Teller distortions[49-50] in **3AMP**. At equilibrium, the average axial Pb-I bond length is shorter than the equatorial Pb-I bond length for both **3AMP** and **4AMP** materials. At RT, **4AMP** remains the same, however, in **3AMP** the average equatorial Pb-I bond length becomes shorter than the average axial bond lengths, Supplemental Table S7. This is one indication that while the Pb-I octahedra are more disordered in **4AMP**, **3AMP** undergoes more obvious structural changes at ambient conditions. In Supplemental Table S2, **3AMP** at equilibrium has a shorter average N-H···I bond length than **4AMP**, which might be the origin of dynamically enhanced organic-inorganic sublattice coupling. When calculating the root-mean-square deviation of distances between atoms within the simulation cells, there is much more variation along the MD trajectory for **3AMP**, Supplemental Figure S7. The larger structural dynamical change leads to larger orbital energy fluctuations along the MD trajectory of **3AMP**, Figure 3. This difference in energy fluctuations is relevant to the dephasing time, which we discuss below.

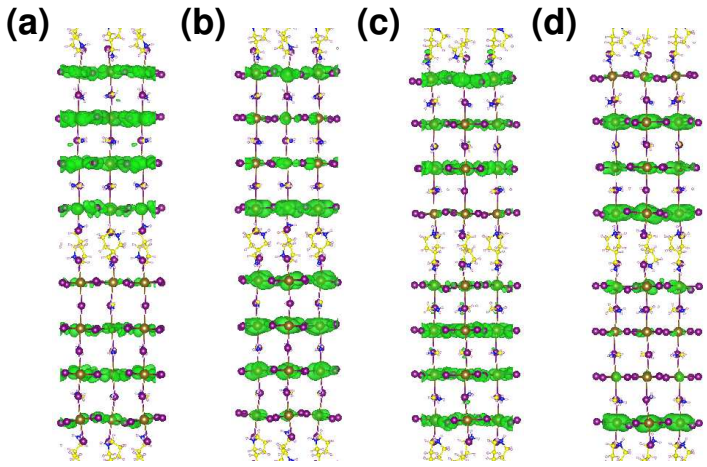

Figure 2. Average partial (band decomposed) charge distribution (without SOC) at the Γ point of (a) VBM and (b) CBM of **3AMP** at room temperature. (c) and (d) show the same but for **4AMP**.

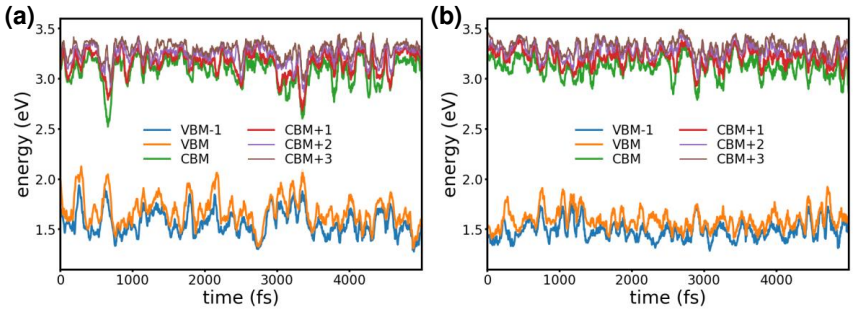

Figure 3. Orbital energy distribution along MD trajectory of **3AMP** (left) and **4AMP** (right) calculated from VBM-1 to CBM+3. The band gap fluctuations are 0.25 and 0.17 eV, respectively.

We next perform NAMD simulations to investigate the nonradiative recombination of charge carriers near the band edges of DJ-phase perovskites. Here, we only consider the intrinsic nonradiative processes (extrinsic processes, such as doping/defects induced carrier trapping, are not included). Since our simulations are performed around RT, we include all energy states within 0.025 eV from the band edges in our excited state dynamics algorithm. This includes states ranging from VBM-1 to CBM+3. We first estimate the radiative lifetime by applying the Einstein coefficient for spontaneous emission, A_{21} (see SI Computational Methods for details). At this level of theory, we find that both materials have a radiative lifetime on the order of μs (in agreement with experiments[51-52]), and nonradiative lifetimes on the order 10 ns as summarized in Table 2. Thus, we mostly focus on the nonradiative recombination processes in these materials. Note that, multiexciton-driven recombinations have not been considered here.

Table 2. The calculated time-averaged band gaps along the AIMD trajectories, root means square of non-adiabatic coupling constants (NAC) over simulation time, dephasing time (D_{ph}), radiative lifetime (RLT), and nonradiative lifetime (NRLT) for anti-aligned **3AMP** and **4AMP**.

species	BG (eV, 300K)	NAC (meV, rms)	D_{ph} time (fs)	RLT (μs)	NRLT (ns)
3AMP	1.40	0.21	2.69	1.03	8.20
4AMP	1.52	0.19	4.03	1.14	6.51

Excited-state dynamics necessarily involve the coupling of electronic and lattice degrees of freedom. Both elastic and inelastic carrier scattering matter during the electron-phonon process at ambient conditions. The elastic electron-phonon scattering assists the quantum decoherence, resulting in the collapse of superposition to a singular state. The significance and importance of decoherence in condensed-phase nonradiative recombination have been emphasized extensively[53-56]. The interaction between the system and environment dampens the nonadiabatic effects and, consequently, controls the transition rates between electronic states[53]. The decoherence time between electronic states i and j can be obtained as the pure-dephasing time in optical response theory using the second-order cumulant approximation[53],

$$D_{ij}(t) = exp\left(-\frac{1}{\hbar^2}\int_0^t dt' \int_0^{t'} dt'' C_{ij}(t'')\right) \quad (1)$$

$$C_{ij}(t) = \left\langle \delta E_{ij}(t') \, \delta E_{ij}(t - t') \right\rangle_{t'} \quad (2)$$

where $C_{ij}(t)$ is the unnormalized autocorrelation function of thermal bandgap fluctuation δE_{ij} between two states *i* and *j* along the trajectory. The pure dephasing functions are shown in Figure 4 (a). To calculate the pure dephasing times, we fit these functions with a Gaussian function exp(-$0.5(\frac{t}{\tau})^2$). As shown in Table 2, **3AMP** has a pure dephasing time of 2.7 fs that is substantially smaller than 4.0 fs calculated for **4AMP**, being consistent with the fact that the dephasing times are inversely proportional to the magnitude of the electronic energy gap fluctuations[57]. Usually, the fast decoherence process slows the electronic relaxation. This phenomenon can be well understood from the quantum Zeno effect, where a quantum transition halts if the decoherence time is infinitesimal[58-60]. Thus, a shorter dephasing time of **3AMP** points to a slower intrinsic nonradiative recombination.

Given the importance of electron-phonon scattering processes, the numerical study of the phonon modes that are coupled to the electronic degrees of freedom provides an additional description of excited-state dynamics. The rapid decay of coherence analyzed above suggests that many phonon modes are involved in this process. The spectral density, which is the Fourier transform of the normalized autocorrelation function of the band gaps, identifies the active phonon modes that are coupled to the associated electronic transition. Figure 4 (b) shows that for both **3AMP** and **4AMP,** the interband transition couples strongly to many low-frequency phonon modes that appear under 500 cm^{-1}. This is because the band edge states consist of orbitals of heavy atoms, Pb and I that give a strong contribution. **3AMP** generally exhibits a larger magnitude in spectral densities compared to **4AMP**, which indicates a stronger interaction between electron subsystem and phonons in **3AMP**. The major peak (53 cm^{-1}) for the electron-phonon coupling in **3AMP** can be assigned to bending of Pb-I-Pb bonds[49, 61]. The major peak for **4AMP** (13 cm^{-1}) can be assigned to the stretching of Pb-I bonds[49].

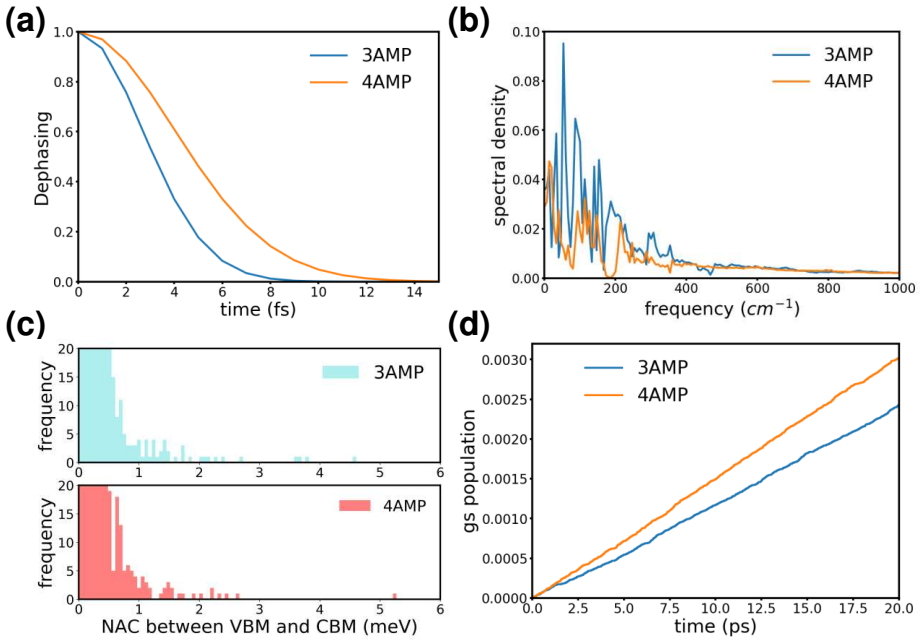

Figure 4. (a) Dephasing functions and (b) the spectral density of the transition between VBM and CBM. (c) The zoomed-in histogram of the full range of NAC values. Plotted NACs have been calculated between VBM and CBM of **3AMP** and **4AMP**. (d) Ground state populations in NAMD relaxation of **3AMP** and **4AMP**.

We now focus on the inelastic electron-phonon scattering that reveals the extent of the exchange of energy between the electronic and vibrational subsystems and consequently affects the recombination processes in materials. The definition of non-adiabatic coupling (NAC)[62] ($d_{ij} \cdot \dot{R}$) between i and j states is as follows,

$$d_{ij} \cdot \dot{R} = \langle \varphi_i | \frac{\partial}{\partial R} | \varphi_j \rangle \dot{R} = \frac{\langle \varphi_i | \nabla_R H | \varphi_j \rangle}{\varepsilon_j - \varepsilon_i} \dot{R} \quad (3)$$

where $\varphi_{i/j}$ are wavefunction of $i^{\text{th}}/j^{\text{th}}$ state of the system, $\dot{R}$ are phonon velocities, and $\varepsilon_{j/i}$ are energies of $i^{\text{th}}/j^{\text{th}}$ states. Since the intra-band relaxations typically happen on hundreds of femtosecond timescales, it is reasonable to assume that all excited carriers relax to the band edges before recombining across the band gap in these two halide perovskites. Generally, the stronger the NAC, the shorter the nonradiative carrier recombination lifetime is. Thus, we focus specifically on the NAC between the states at the band edge. The root means square (RMS) NAC between the VBM and CBM of **3AMP** is 0.21 meV, which is slightly stronger than 0.19 meV calculated for **4AMP**. **4AMP** has a larger time-averaged bandgap than **3AMP** (Table 2) and smaller nuclei position fluctuation (Figure S7). According to equation (3), this is a natural explanation for the smaller NAC value of **4AMP**. Figure 4(c) shows a plotted histogram of the frequency of occurrence NAC values of various strengths, where a high NAC value is empirically defined as

being greater than 0.1 meV. The area under the curve above 0.1 meV is nearly identical for the two materials in question. The NAC values large enough to induce the transition among states have almost the same occurrence in these two materials, as also shown in Supplemental Figure 4 (c). Thus, NAC does not play a decisive role in the determination of the relative rates of nonradiative processes in these two materials.

Based on the analysis above, we find that **3AMP** has a noticeably longer intrinsic nonradiative lifetime when compared with **4AMP**, see Figure 4(d). A faster ground state population growth means indeed faster nonradiative recombination[32, 63]. This difference originates almost exclusively from the difference in the dephasing processes in these halide perovskites. Further, a reduction of an intrinsic nonradiative lifetime may contribute to an overall larger carrier lifetime and V_{oc} of **3AMP** as found in previous experimental work[29].

In summary, our time-dependent ab initio NAMD modeling work shines some light on how intrinsic electron-lattice dynamics may affect solar cell device performance for 3AMP and 4AMP perovskite devices. In solar cells, the efficiency is strongly relevant to the dynamics of photoexcited charge carriers. It is important to get an estimation of the timescale of electron-hole recombination and pathways using theoretical and simulation aspects. The current NAMD method we adopted in this work provides a good option, which is also applicable to other 2D hybrid organic-inorganic perovskites. The larger structural dynamics of **3AMP** lead to more obvious state energy fluctuation near the band edges and further result in a faster loss of coherence. Combined with nearly identical band gaps and nonadiabatic coupling constants, the faster decoherence of **3AMP** leads to a longer intrinsic nonradiative lifetime, which might be a partial explanation for the experimentally higher PCE and performance in solar cells of **3AMP**. The energy transfer between electronic and vibrational subsystems is substantially weakened and inhibits the energy loss in these two systems, which leads to longer nonradiative lifetimes. Both materials have an extremely long (microseconds) radiative lifetime at the chosen level of theory. The intense structural fluctuation of 2D DJ perovskites accelerates the decoherence process, leading to slower intrinsic nonradiative recombination, which is beneficial for optoelectronic performances. Our simulations further relate the band-gap sensitivity to a presence of a specific organic cation. But other practical aspects are related to the choice of the organic cation including the material growth: 4AMP-based DJ pure phase crystals have been synthesized up to n=7 like BA-based RP phases[47]. The easy growth of 4AMP DJ phases with large n by comparison to 3AMP is attributed to a reduced accumulation of strain within the 4AMP-DJ lattices at room temperature for intermediate n values[27-28], related to a very small lattice mismatch between the n=1 compound and the 3D perovskite. On the other hand, longer carrier lifetimes may be a natural explanation for the superior photovoltaic performances of **3AMP** based solar cells, which exhibit a larger open-circuit voltage (V_{oc}) than their **4AMP** based counterparts. In addition, the larger short-circuit current (J_{sc}) for **3AMP** was attributed to an enhanced carrier transport due to shorter interlayer I-I distances and smaller effective masses[29]. This leads to insight into ways to engineer even better-performing devices. Possible interlayer cation engineering or design could be: finding interlayer cations which lead to shorter X···X (X=halide) distance[30]. Or shortening the I-I distance by replacing the single-band ring of 3AMP/4AMP with a benzene ring[64]. Thus, observed atomic-scale insights on the relationship between the dynamic structure and charge carrier recombination processes may help the community to screen a variety of mono- and di-cationic spacer molecules to optimize the optoelectronic properties of 2D-halide perovskites, in addition to constraints related to material

growth and heterostructure optimization for device applications. Overall this work provides valuable guiding principles for experimentalists when choosing 2D perovskite materials for optoelectronic applications.

SUPPLEMENTARY MATERIAL

Detailed computational method, structure, partial (band decomposed) charge densities, density of states, band structures of aligned and anti-aligned 3AMP and 4AMP, data for total energies, Pb-I-Pb angles, N-H···I bond lengths, effective masses for different systems.

AUTHOR INFORMATION

Corresponding Authors

*E-mail: dibyajnc@gmail.com andajneukirch@lanl.gov

Author Contributions

All authors have approved the final version of the manuscript.

ACKNOWLEDGMENT

The work at Los Alamos National Laboratory (LANL) was supported by the LANL LDRD program (S.G.L, F.L, W.N. A.J.N., and S.T.). This work was done in part at Center for Nonlinear Studies (CNLS) and the Center for Integrated Nanotechnologies CINT), a U.S. Department of Energy and Office of Basic Energy Sciences user facility, at LANL. This research used resources provided by the LANL Institutional Computing Program. LANL is operated by Triad National Security, LLC, for the National Nuclear Security Administration of the U.S. Department of Energy under contract no. 89233218NCA000001. J.E acknowledges the financial support from the Institut Universitaire de France. Y. W. and O. V. P. acknowledge support of the U. S. Department of Energy, grant No. DE-SC0014429.

References:

1. Jošt, M.; Köhnen, E.; Morales-Vilches, A. B.; Lipovšek, B.; Jäger, K.; Macco, B.; Al-Ashouri, A.; Krč, J.; Korte, L.; Rech, B., Textured interfaces in monolithic perovskite/silicon tandem solar cells: advanced light management for improved efficiency and energy yield. *Energy & Environmental Science* **2018,** *11* (12), 3511-3523.
2. Laboratory, N. R. E. Best Research-Cell Efficiency Chart. https://www.nrel.gov/pv/cell-efficiency.html

(accessed May 05, 2021).
3. Niu, G.; Guo, X.; Wang, L., Review of recent progress in chemical stability of perovskite solar cells. *J. Mater. Chem. A* **2015,** *3* (17), 8970-8980.
4. Asghar, M.; Zhang, J.; Wang, H.; Lund, P., Device stability of perovskite solar cells–A review. *Renewable and Sustainable Energy Reviews* **2017,** *77*, 131-146.
5. Park, N.-G., Perovskite solar cells: an emerging photovoltaic technology. *Materials today* **2015,** *18* (2), 65-72.
6. Ava, T. T.; Al Mamun, A.; Marsillac, S.; Namkoong, G., A review: thermal stability of methylammonium lead halide based perovskite solar cells. *Applied Sciences* **2019,** *9* (1), 188.
7. Ansari, M. I. H.; Qurashi, A.; Nazeeruddin, M. K., Frontiers, opportunities, and challenges in perovskite solar cells: A critical review. *Journal of Photochemistry and Photobiology C: Photochemistry Reviews* **2018,** *35*, 1-24.
8. Fu, Y.; Hautzinger, M. P.; Luo, Z.; Wang, F.; Pan, D.; Aristov, M. M.; Guzei, I. A.; Pan, A.; Zhu, X.; Jin, S., Incorporating large A cations into lead iodide perovskite cages: Relaxed goldschmidt tolerance factor and impact on exciton–phonon interaction. *ACS central science* **2019,** *5* (8), 1377-1386.
9. Kieslich, G.; Sun, S.; Cheetham, A. K., An extended tolerance factor approach for organic–inorganic perovskites. *Chemical science* **2015,** *6* (6), 3430-3433.
10. Pedesseau, L.; Sapori, D.; Traore, B.; Robles, R.; Fang, H. H.; Loi, M. A.; Tsai, H. H.; Nie, W. Y.; Blancon, J. C.; Neukirch, A.; Tretiak, S.; Mohite, A. D.; Katan, C.; Even, J.; Kepenekian, M., Advances and Promises of Layered Halide Hybrid Perovskite Semiconductors. *Acs Nano* **2016,** *10* (11), 9776-9786.
11. Zhou, C. K.; Lin, H. R.; He, Q. Q.; Xu, L. J.; Worku, M.; Chaaban, M.; Lee, S.; Shi, X. Q.; Du, M. H.; Ma, B. W., Low dimensional metal halide perovskites and hybrids. *Materials Science & Engineering R-Reports* **2019,** *137*, 38-65.
12. Krishna, A.; Gottis, S.; Nazeeruddin, M. K.; Sauvage, F., Mixed Dimensional 2D/3D Hybrid Perovskite Absorbers: The Future of Perovskite Solar Cells? *Adv. Funct. Mater.* **2019,** *29* (8).
13. Grancini, G.; Nazeeruddin, M. K., Dimensional tailoring of hybrid perovskites for photovoltaics. *Nature Reviews Materials* **2019,** *4* (1), 4-22.
14. Shi, E. Z.; Gao, Y.; Finkenauer, B. P.; Akriti; Coffey, A. H.; Dou, L. T., Two-dimensional halide perovskite nanomaterials and heterostructures. *Chemical Society Reviews* **2018,** *47* (16), 6046-6072.
15. Katan, C.; Mercier, N.; Even, J., Quantum and dielectric confinement effects in lower-dimensional hybrid perovskite semiconductors. *Chemical reviews* **2019,** *119* (5), 3140-3192.
16. Li, X.; Hoffman, J. M.; Kanatzidis, M. G., The 2D Halide Perovskite Rulebook: How the Spacer Influences Everything from the Structure to Optoelectronic Device Efficiency. *Chemical reviews* **2021,** *121* (4), 2230-2291.
17. Zhang, F.; Kim, D. H.; Lu, H.; Park, J.-S.; Larson, B. W.; Hu, J.; Gao, L.; Xiao, C.; Reid, O. G.; Chen, X., Enhanced charge transport in 2D perovskites via fluorination of organic cation. *Journal of the American Chemical Society* **2019,** *141* (14), 5972-5979.
18. Milot, R. L.; Sutton, R. J.; Eperon, G. E.; Haghighirad, A. A.; Martinez Hardigree, J.; Miranda, L.; Snaith, H. J.; Johnston, M. B.; Herz, L. M., Charge-carrier dynamics in 2D hybrid metal–halide perovskites. *Nano Lett.* **2016,** *16* (11), 7001-7007.
19. Smith, I. C.; Hoke, E. T.; Solis-Ibarra, D.; McGehee, M. D.; Karunadasa, H. I., A layered hybrid perovskite solar-cell absorber with enhanced moisture stability. *Angewandte Chemie International Edition* **2014,** *53* (42), 11232-11235.
20. Zhang, J.; Qin, J.; Wang, M.; Bai, Y.; Zou, H.; Keum, J. K.; Tao, R.; Xu, H.; Yu, H.; Haacke, S., Uniform permutation of quasi-2D perovskites by vacuum poling for efficient, high-fill-factor solar cells. *Joule* **2019,** *3* (12), 3061-3071.
21. Luo, T.; Zhang, Y.; Xu, Z.; Niu, T.; Wen, J.; Lu, J.; Jin, S.; Liu, S.; Zhao, K., Compositional Control in 2D Perovskites with Alternating Cations in the Interlayer Space for Photovoltaics with Efficiency over 18%. *Adv. Mater.* **2019,** *31* (44), 1903848.
22. Wu, G.; Li, X.; Zhou, J.; Zhang, J.; Zhang, X.; Leng, X.; Wang, P.; Chen, M.; Zhang, D.; Zhao, K., Fine multi-phase Alignments in 2D perovskite solar cells with efficiency over 17% via slow post-annealing. *Adv. Mater.* **2019,** *31* (42), 1903889.
23. Zuo, C.; Scully, A. D.; Vak, D.; Tan, W.; Jiao, X.; McNeill, C. R.; Angmo, D.; Ding, L.; Gao, M., Self-assembled 2D perovskite layers for efficient printable solar cells. *Advanced Energy Materials* **2019,** *9* (4), 1803258.
24. Calabrese, J.; Jones, N.; Harlow, R.; Herron, N.; Thorn, D.; Wang, Y., Preparation and characterization of

layered lead halide compounds. *Journal of the American Chemical Society* **1991,** *113* (6), 2328-2330.
25. Li, Y.; Milić, J. V.; Ummadisingu, A.; Seo, J.-Y.; Im, J.-H.; Kim, H.-S.; Liu, Y.; Dar, M. I.; Zakeeruddin, S. M.; Wang, P., Bifunctional organic spacers for formamidinium-based hybrid Dion–Jacobson two-dimensional perovskite solar cells. *Nano Lett.* **2018,** *19* (1), 150-157.
26. Quan, L. N.; Yuan, M.; Comin, R.; Voznyy, O.; Beauregard, E. M.; Hoogland, S.; Buin, A.; Kirmani, A. R.; Zhao, K.; Amassian, A., Ligand-stabilized reduced-dimensionality perovskites. *Journal of the American Chemical Society* **2016,** *138* (8), 2649-2655.
27. Kepenekian, M.; Traore, B.; Blancon, J.-C.; Pedesseau, L.; Tsai, H.; Nie, W.; Stoumpos, C. C.; Kanatzidis, M. G.; Even, J.; Mohite, A. D., Concept of lattice mismatch and emergence of surface states in two-dimensional hybrid perovskite quantum wells. *Nano Lett.* **2018,** *18* (9), 5603-5609.
28. Blancon, J.-C.; Even, J.; Stoumpos, C. C.; Kanatzidis, M. G.; Mohite, A. D., Semiconductor physics of organic–inorganic 2D halide perovskites. *Nature nanotechnology* **2020,** *15* (12), 969-985.
29. Mao, L.; Ke, W.; Pedesseau, L.; Wu, Y.; Katan, C.; Even, J.; Wasielewski, M. R.; Stoumpos, C. C.; Kanatzidis, M. G., Hybrid Dion–Jacobson 2D lead iodide perovskites. *Journal of the American Chemical Society* **2018,** *140* (10), 3775-3783.
30. Cohen, B.-E.; Li, Y.; Meng, Q.; Etgar, L., Dion–Jacobson two-dimensional perovskite solar cells based on benzene dimethanammonium cation. *Nano Lett.* **2019,** *19* (4), 2588-2597.
31. Tsai, H.; Nie, W.; Blancon, J.-C.; Stoumpos, C. C.; Asadpour, R.; Harutyunyan, B.; Neukirch, A. J.; Verduzco, R.; Crochet, J. J.; Tretiak, S., High-efficiency two-dimensional Ruddlesden–Popper perovskite solar cells. *Nature* **2016,** *536* (7616), 312-316.
32. Ghosh, D.; Acharya, D.; Pedesseau, L.; Katan, C.; Even, J.; Tretiak, S.; Neukirch, A. J., Charge carrier dynamics in two-dimensional hybrid perovskites: Dion–Jacobson vs. Ruddlesden–Popper phases. *J. Mater. Chem. A* **2020,** *8* (42), 22009-22022.
33. Ahmad, S.; Fu, P.; Yu, S.; Yang, Q.; Liu, X.; Wang, X.; Wang, X.; Guo, X.; Li, C., Dion-Jacobson phase 2D layered perovskites for solar cells with ultrahigh stability. *Joule* **2019,** *3* (3), 794-806.
34. Gong, X.; Voznyy, O.; Jain, A.; Liu, W.; Sabatini, R.; Piontkowski, Z.; Walters, G.; Bappi, G.; Nokhrin, S.; Bushuyev, O., Electron–phonon interaction in efficient perovskite blue emitters. *Nature materials* **2018,** *17* (6), 550-556.
35. Park, I.-H.; Zhang, Q.; Kwon, K. C.; Zhu, Z.; Yu, W.; Leng, K.; Giovanni, D.; Choi, H. S.; Abdelwahab, I.; Xu, Q.-H., Ferroelectricity and Rashba effect in a two-dimensional Dion-Jacobson hybrid organic–inorganic perovskite. *Journal of the American Chemical Society* **2019,** *141* (40), 15972-15976.
36. Kang, J.; Wang, L.-W., Dynamic Disorder and Potential Fluctuation in Two-Dimensional Perovskite. *The journal of physical chemistry letters* **2017,** *8* (16), 3875-3880.
37. Even, J.; Pedesseau, L.; Jancu, J.-M.; Katan, C., Importance of spin–orbit coupling in hybrid organic/inorganic perovskites for photovoltaic applications. *The Journal of Physical Chemistry Letters* **2013,** *4* (17), 2999-3005.
38. Pedesseau, L.; Jancu, J.-M.; Rolland, A.; Deleporte, E.; Katan, C.; Even, J., Electronic properties of 2D and 3D hybrid organic/inorganic perovskites for optoelectronic and photovoltaic applications. *Optical and Quantum Electronics* **2014,** *46* (10), 1225-1232.
39. Even, J.; Pedesseau, L.; Jancu, J. M.; Katan, C., DFT and k· p modelling of the phase transitions of lead and tin halide perovskites for photovoltaic cells. *physica status solidi (RRL)–Rapid Research Letters* **2014,** *8* (1), 31-35.
40. Meggiolaro, D.; De Angelis, F., First-principles modeling of defects in lead halide perovskites: best practices and open issues. *ACS Energy Letters* **2018,** *3* (9), 2206-2222.
41. Ghosh, D.; Smith, A. R.; Walker, A. B.; Islam, M. S., Mixed A-cation perovskites for solar cells: atomic-scale insights into structural distortion, hydrogen bonding, and electronic properties. *Chemistry of Materials* **2018,** *30* (15), 5194-5204.
42. Ghosh, D.; Aziz, A.; Dawson, J. A.; Walker, A. B.; Islam, M. S., Putting the squeeze on lead iodide perovskites: pressure-induced effects to tune their structural and optoelectronic behavior. *Chemistry of Materials* **2019,** *31* (11), 4063-4071.
43. Onida, G.; Reining, L.; Rubio, A., Electronic excitations: density-functional versus many-body Green's-function approaches. *Reviews of modern physics* **2002,** *74* (2), 601.
44. Fu, Y.; Jiang, X.; Li, X.; Traoré, B.; Spanopoulos, I.; Katan, C.; Even, J.; Kanatzidis, M. G.; Harel, E., Cation Engineering in Two-Dimensional Ruddlesden–Popper Lead Iodide Perovskites with Mixed Large A-Site Cations in the Cages. *Journal of the American Chemical Society* **2020,** *142* (8), 4008-4021.

45. Perdew, J. P.; Levy, M., Physical content of the exact Kohn-Sham orbital energies: band gaps and derivative discontinuities. *Physical Review Letters* **1983,** *51* (20), 1884.
46. Perdew, J. P., Density functional theory and the band gap problem. *International Journal of Quantum Chemistry* **1985,** *28* (S19), 497-523.
47. Mao, L.; Kennard, R. M.; Traore, B.; Ke, W.; Katan, C.; Even, J.; Chabinyc, M. L.; Stoumpos, C. C.; Kanatzidis, M. G., Seven-layered 2D hybrid lead iodide perovskites. *Chem* **2019,** *5* (10), 2593-2604.
48. Cheng, B.; Li, T.-Y.; Wei, P.-C.; Yin, J.; Ho, K.-T.; Retamal, J. R. D.; Mohammed, O. F.; He, J.-H., Layer-edge device of two-dimensional hybrid perovskites. *Nature communications* **2018,** *9* (1), 1-7.
49. Park, M.; Neukirch, A. J.; Reyes-Lillo, S. E.; Lai, M.; Ellis, S. R.; Dietze, D.; Neaton, J. B.; Yang, P.; Tretiak, S.; Mathies, R. A., Excited-state vibrational dynamics toward the polaron in methylammonium lead iodide perovskite. *Nature communications* **2018,** *9* (1), 1-9.
50. Neukirch, A. J.; Abate, I. I.; Zhou, L.; Nie, W.; Tsai, H.; Pedesseau, L.; Even, J.; Crochet, J. J.; Mohite, A. D.; Katan, C., Geometry distortion and small polaron binding energy changes with ionic substitution in halide perovskites. *The journal of physical chemistry letters* **2018,** *9* (24), 7130-7136.
51. DeQuilettes, D. W.; Koch, S.; Burke, S.; Paranji, R. K.; Shropshire, A. J.; Ziffer, M. E.; Ginger, D. S., Photoluminescence lifetimes exceeding 8 μs and quantum yields exceeding 30% in hybrid perovskite thin films by ligand passivation. *ACS Energy Letters* **2016,** *1* (2), 438-444.
52. Yang, X.; Fu, Y.; Su, R.; Zheng, Y.; Zhang, Y.; Yang, W.; Yu, M.; Chen, P.; Wang, Y.; Wu, J., Superior Carrier Lifetimes Exceeding 6 μs in Polycrystalline Halide Perovskites. *Adv. Mater.* **2020,** *32* (39), 2002585.
53. Jaeger, H. M.; Fischer, S.; Prezhdo, O. V., Decoherence-induced surface hopping. *The Journal of chemical physics* **2012,** *137* (22), 22A545.
54. Zhu, C., Restoring electronic coherence/decoherence for a trajectory-based nonadiabatic molecular dynamics. *Scientific reports* **2016,** *6* (1), 1-8.
55. Kang, J.; Wang, L.-W., Nonadiabatic molecular dynamics with decoherence and detailed balance under a density matrix ensemble formalism. *Physical Review B* **2019,** *99* (22), 224303.
56. Agrawal, S.; Lin, W.; Prezhdo, O. V.; Trivedi, D. J., Ab initio quantum dynamics of charge carriers in graphitic carbon nitride nanosheets. *The Journal of Chemical Physics* **2020,** *153* (5), 054701.
57. Akimov, A. V.; Prezhdo, O. V., Persistent electronic coherence despite rapid loss of electron–nuclear correlation. *The Journal of Physical Chemistry Letters* **2013,** *4* (22), 3857-3864.
58. Itano, W. M.; Heinzen, D. J.; Bollinger, J.; Wineland, D., Quantum zeno effect. *Physical Review A* **1990,** *41* (5), 2295.
59. Prezhdo, O. V.; Rossky, P. J., Relationship between quantum decoherence times and solvation dynamics in condensed phase chemical systems. *Physical review letters* **1998,** *81* (24), 5294.
60. Prezhdo, O. V., Quantum anti-zeno acceleration of a chemical reaction. *Physical review letters* **2000,** *85* (21), 4413.
61. Pérez-Osorio, M. A.; Milot, R. L.; Filip, M. R.; Patel, J. B.; Herz, L. M.; Johnston, M. B.; Giustino, F., Vibrational properties of the organic–inorganic halide perovskite CH3NH3PbI3 from theory and experiment: factor group analysis, first-principles calculations, and low-temperature infrared spectra. *The Journal of Physical Chemistry C* **2015,** *119* (46), 25703-25718.
62. Tully, J. C., Molecular dynamics with electronic transitions. *The Journal of Chemical Physics* **1990,** *93* (2), 1061-1071.
63. Ghosh, D.; Acharya, D.; Zhou, L.; Nie, W.; Prezhdo, O. V.; Tretiak, S.; Neukirch, A. J., Lattice Expansion in Hybrid Perovskites: Effect on Optoelectronic Properties and Charge Carrier Dynamics. *The Journal of Physical Chemistry Letters* **2019,** *10* (17), 5000-5007.
64. Li, X.; Ke, W.; Traoré, B.; Guo, P.; Hadar, I.; Kepenekian, M.; Even, J.; Katan, C.; Stoumpos, C. C.; Schaller, R. D., Two-dimensional Dion–Jacobson hybrid lead iodide perovskites with aromatic diammonium cations. *Journal of the American Chemical Society* **2019,** *141* (32), 12880-12890.

PLEASE CITE THIS ARTICLE AS DOI: 10.1063/5.0066087

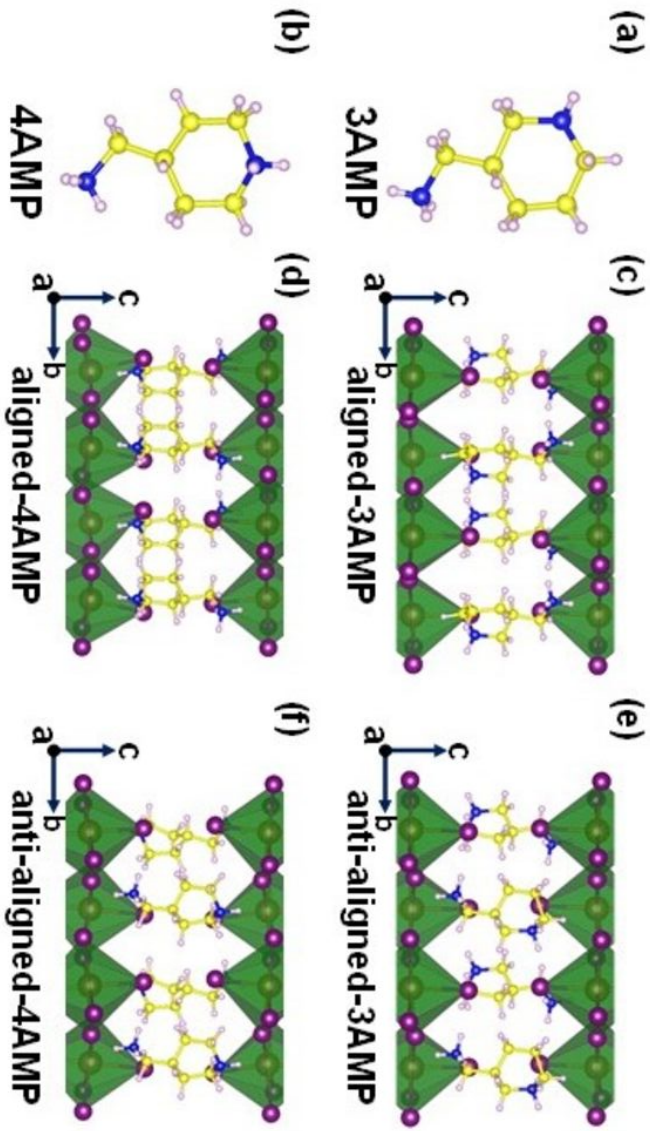

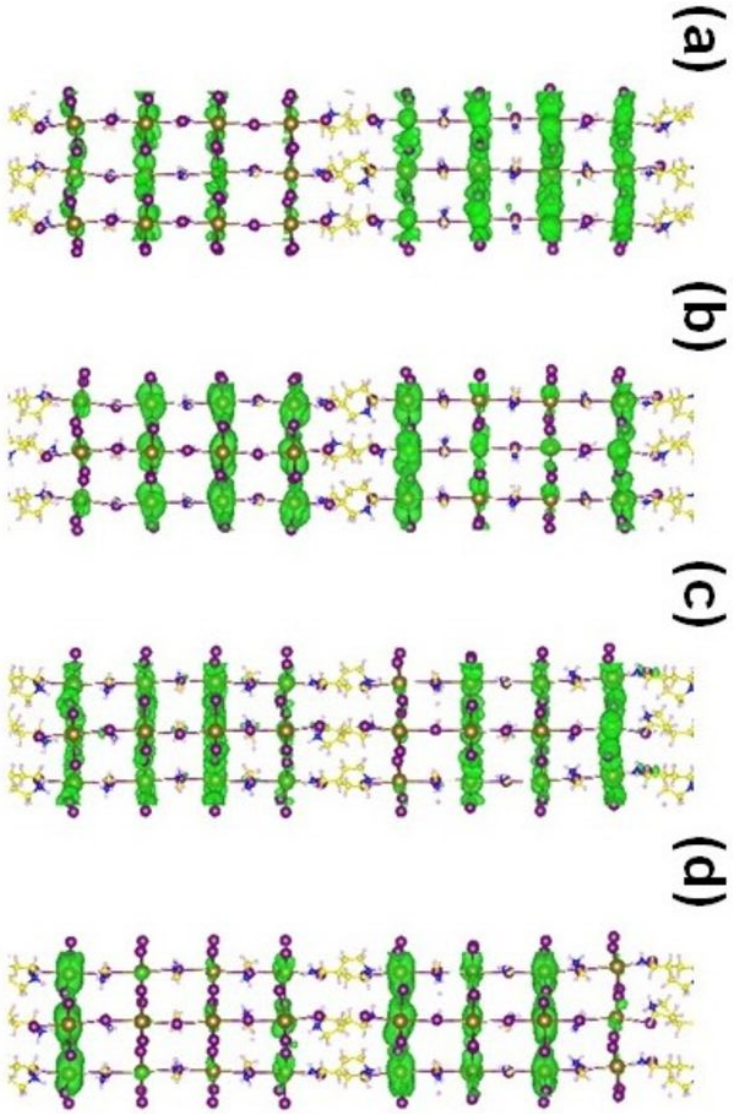

AIP Publishing

Applied Physics Letters ACCEPTED MANUSCRIPT

PLEASE CITE THIS ARTICLE AS DOI: 10.1063/5.0066087